Titel/Title: Channel inception through bottom-current erosion of pockmarks revealed by numerical simulation

Autor*innen/Author(s): Kaiqi Yu, Alice Lefebvre, Wei Li, Wenhuan Zhan, Elda Miramontes

Veröffentlichungsversion/Published version: Postprint

Publikationsform/Type of publication: Artikel/Aufsatz

Empfohlene Zitierung/Recommended citation:

Yu, K., Lefebvre, A., Li, W., Zhan, W. & Miramontes, E. (2023) Channel inception through bottom-current erosion of pockmarks revealed by numerical simulation. Earth Surface Processes and Landforms, 1– 14. Available from: https://doi.org/10.1002/esp.5610

Verfügbar unter/Available at:
(wenn vorhanden, bitte den DOI angeben/please provide the DOI if available)

https://doi.org/10.1002/esp.5610

Zusätzliche Informationen/Additional information:

Channel Inception Through Bottom Current Erosion of Pockmarks Revealed by Numerical Simulation

Kaiqi Yu[1, 2, 3, 4], Alice Lefebvre[3], Wei Li[1, 2 *], Wenhuan Zhan[1, 2], Elda Miramontes[3, 4]

1 Key Laboratory of Ocean and Marginal Sea Geology, South China Sea Institute of Oceanology, Innovation Academy of South China Sea Ecology and Environmental Engineering, Chinese Academy of Sciences, Guangzhou 510301, China

2 University of Chinese Academy of Sciences, Beijing 100049, China

3 MARUM-Center for Marine Environmental Sciences, University of Bremen, Bremen 28359, Germany

4 Faculty of Geosciences, University of Bremen, Bremen 28359, Germany

Corresponding to: Dr. Wei Li (wli@scsio.ac.cn)

Abstract

In deep-marine environments, the inception of channels can be induced by the interaction between bottom currents and rough topography. However, it is still unclear under which conditions such features can form and what happens in the earliest phase of channel development. In this study, based on the morphological, sedimentary and oceanographic settings of a pockmark field in the NW South China Sea, we reveal the process of channel inception through the erosion of pockmarks by bottom currents. Using numerical simulations, we show that an appropriate current velocity can induce the erosion of pockmark trains in cohesive sediments, leading to the coalescence of discrete pockmarks and the formation of a channel with a rough thalweg. The interaction of bottom currents with the pockmarks induces a significant erosion along the pockmarks axis. Bottom current erosion is strongest at the downstream edges of pockmarks, where the horizontal velocity reaches a maximum and an upwelling forms. Erosion increases as the distance between pockmarks reduces. In our simulation results, a channel is only formed by the coalescence of pockmarks if the distance between pockmarks is <6 times the diameter of the pockmark. This study provides evidence of the formation of channels by bottom currents, which helps reconstruct paleoceanographic conditions based on sediment architecture. It also shows the complex hydrodynamics at these structures that strongly control sedimentary processes and may affect distribution of benthic ecosystems in marine environments.

Keywords: Channel inception, Bottom current erosion, Pockmark, Numerical simulation, Morphological evolution.

1. INTRODUCTION

Channels are prominent topographic features on the seafloor of continental slopes and basin plains. Their inception and evolution significantly control sediment transport and deposition in deep-water environments (Stow and Mayall, 2000; Habgood et al., 2003; Posamentier and Kolla, 2003). Along-slope bottom currents (e.g. contour currents) and down-slope turbidity currents are considered as two of the main mechanisms controlling or influencing the development of deep-water channels (Peakall et al., 2007; Stow et al., 2009; Rebesco et al., 2014; Peakall and Sumner, 2015; Miramontes et al., 2019a; 2020). Channels formed by down-slope gravity-driven processes are commonly defined as “submarine channels”, and their inception can happen either through erosion (i.e. slope channel incision, Fildani et al., 2013; Covault et al., 2014) and/or deposition (i.e. forming channel levees and flow confinement, de Leeuw et al., 2016) by turbidity currents. Near-bed currents, generally observed at within 100 m above the seafloor (e.g. Miramontes et al., 2019b; Fuhrmann et al., 2020; Ye et al., 2023), induced by oceanographic processes (i.e. bottom currents) can be accelerated by topographic obstacles, resulting in seafloor erosion and the formation of channels (or moats) that are commonly parallel to the bathymetric contours (Miramontes et al., 2021; Wilckens et al., 2021; 2023). However, bottom-current-related channels can also be found away from topographic obstacles (Fig. 1), and their inception is still poorly understood.

Pockmarks are “crater-like” depressions on the seafloor formed by fluid seepage, which have been observed worldwide and often coexist with channels (Pilcher and Argent, 2007; Cartwright and Santamarina, 2015; Yu et al., 2021). In several areas around the world, it has been suggested that pockmarks can be enlarged (Michaud et al., 2018), reshaped (Cukur et al., 2019) and elongated (Andresen et al., 2008) by bottom-current action (Fig. 1). Based on geophysical data analyses, Kilhams et al. (2011) and Yu et al. (2021) demonstrated that the inception of bottom-current-related channel might be initiated from pockmarks that are trail-aligned parallel to the seafloor contours. However, the specific processes of channel inception from pockmarks are still unknown. This study aims to reconstruct the morphological evolution of pockmarks controlled by bottom currents through numerical simulations based on seafloor observations from the NW South China Sea (Fig. 1C), and to decipher the hydrodynamic conditions that are necessary for channel inception. The reconstructed along-slope evolutionary processes from pockmarks to channel confinements will not only contribute to the recognition of bottom-current genesis for channel inception, but also provide important implications for understanding the development of pockmark-related benthic ecosystems and reconstructing paleoceanography and paleoenvironment.

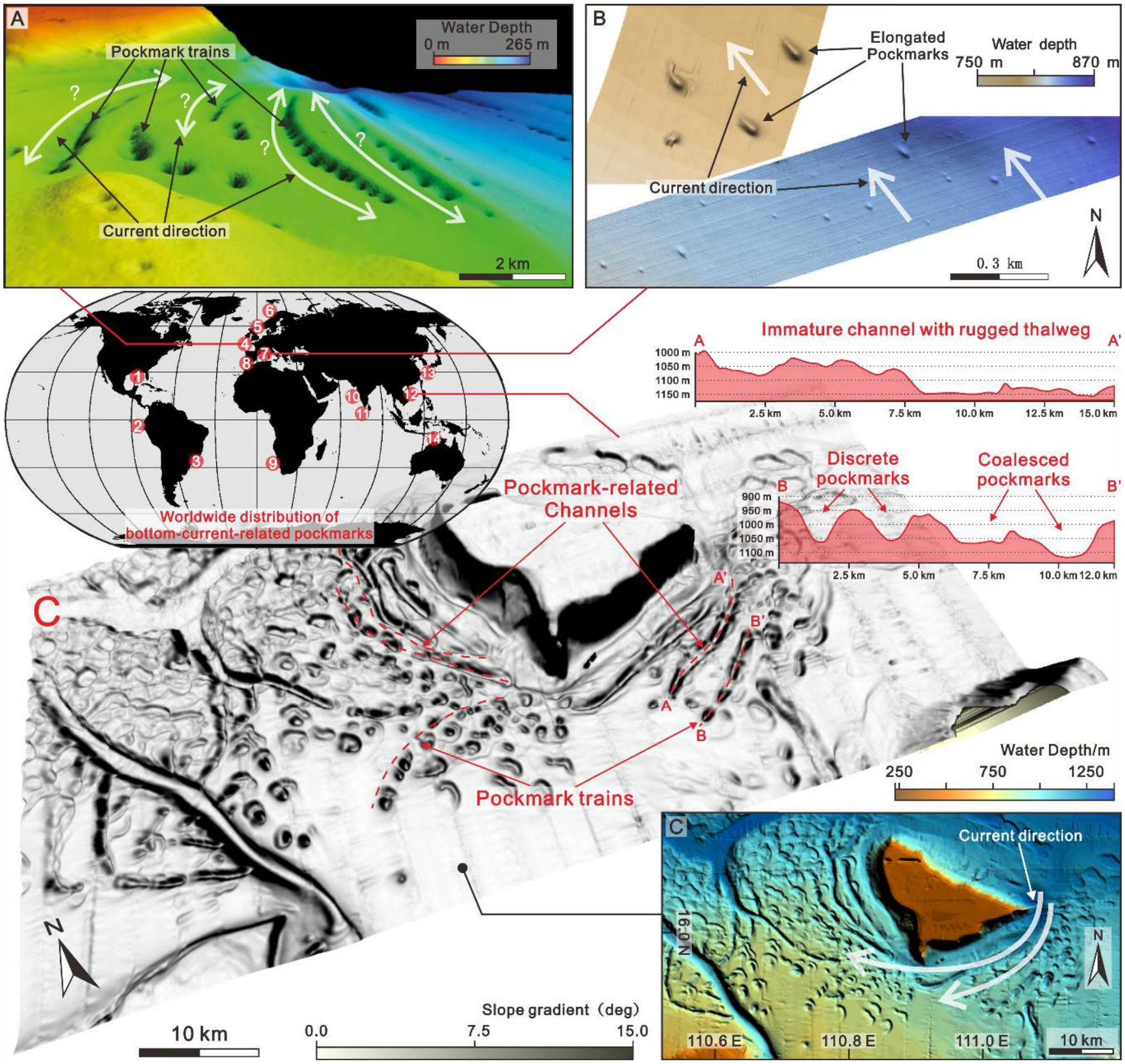

Figure 1. Examples of pockmarks influenced by bottom currents, and their locations. 1. Gulf of Mexico (Davies et al., 2010); 2. Carnegie Ridge Offshore Ecuador (Michaud et al., 2018); 3. SE Brazilian Continental Margin (Berton and Vesely, 2018); 4. Alongslope pockmark trains at the western shelf of Scotland (shown as fig. 1A modified from Audsley et al., 2019); 5. Danish North Sea (Andresen et al., 2008); 6. Western Continental Margin of Norway (Webb et al., 2009); 7. Elongated pockmarks in the NW Mediterranean Sea (shown as fig. 1B modified from Miramontes et al., 2019a); 8. Strait of Gibraltar (León et al., 2014); 9. Namibia Continental Margin (Wenau et al., 2021); 10. Western Indian Continental Margin (Dandapath et al., 2010); 11. Maldives, Indian Ocean (Betzler et al., 2011); 12. Pockmark field in the NW South China Sea (shown as Fig. 1C, modified from Yu et al., 2021); 13. SE Korean Continental Shelf (Cukur et al., 2019); 14. NW Australian Continental Margin (Picard et al., 2018).

2. GEOLOGICAL SETTING

In this study, the settings of the numerical simulation are based on the sedimentological and oceanographic conditions of a pockmark field located in the southwest of Xisha Archipelago, South China Sea (Fig. 2). In the Xisha Archipelago, active fluid seepage and wide development of pathways, i.e. faults, gas chimneys and pipe structures within the underlying strata, jointly predefine the weakness zones and precondition the pockmark formation (Sun et al., 2011; Chen et al., 2018).

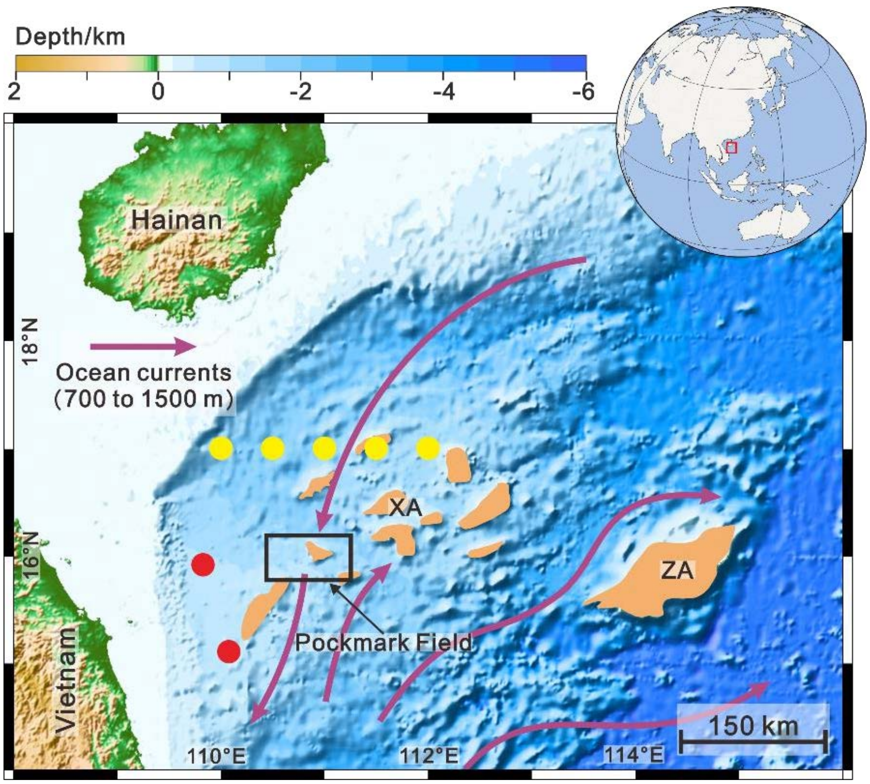

Figure 2. Bathymetric and topographic map of the northwestern South China Sea, showing the location of the pockmark field. Sediment cores (red dots) and in-situ measurements for current velocity (yellow dots) are cited from Astakhov (2004) and Yang et al. (2019), respectively. The purple arrows indicate the simulated ocean currents at water depth between 700 to 1500 m from Quan and Xue (2018). XA, Xisha Archipelago; ZA, Zhongsha Archipelago.

2.1 Sedimentology

According to the bottom sediment dataset collected by Astakhov (2004), in the NW South China Sea (Fig. 2), surface and subsurface sediments (down to 3 m below the seafloor) are dominated by very fine silt, which shows a seafloor composed of cohesive sediments (median grain diameter D50 = ~50 μm) with mainly silt (66%), clay (28%) and some sand (6%). Moreover, the abundant published grain size data from surface sediments of the continental shelf and slope of the northern South China Sea confirmed that the zones below 200 m water depth are commonly dominated by sediments with mean grain sizes ranging between 4 and 20 μm (Zhong et al., 2017). We can thus assume that the sediments in the pockmark field of this study are cohesive sediments mainly composed of silt.

In the Xisha Archipelago, carbonate biogenic materials forms around the carbonate reefs, occupying a high percentage (ca. 54%) in the surface sediments adjacent to the reefs (Liu et al., 2013, Yi et al., 2018). The high percentage of biogenic materials may increase sediment grain size and alter sediment properties. However, the percentage of biogenic material significantly declines in the deeper region, away from the carbonate reefs (Liu et al., 2014; Zhang et al., 2015). In this study, we aim to reveal the evolution of pockmarks away from topographic obstacles, hence the impact of biogenic materials has been disregarded.

2.2 Oceanography

The South China Sea is composed of four main water masses: surface water (at a water depth between 0 and 750 m), intermediate water (at water depths between 750 and 1500 m), deep and bottom waters below 1,500 m (Liu et al., 2008; Yin et al., 2021). The pockmark field is located in the northwestern South China Sea at water depths ranging from 750 to 1300 m (Figs. 1 and 2), and thus under the influence of the intermediate water mass. According to the layered circulation model of the South China Sea proposed by Quan and Xue (2018), ocean currents flow through the pockmark field with a southwestward direction (Fig. 2). Furthermore, vessel-mounted ADCP data from Yang et al. (2019) shows a variable speed of ocean currents relatively close to the pockmark field, with an average speed ranging from 10 to 20 cm/s and maximum speed of ca. 80 cm/s.

3. METHODOLOGY

The numerical model of this study is set up with the Delft3D modeling system (Deltares, 2014) that solves the equations of horizontal momentum, continuity, and transport on a staggered model grid using an implicit finite-difference scheme (Lesser et al., 2004). In this study, setup of the numerical simulation includes bathymetric setting, sensitivity analysis of input parameters and modelling processes. The sensitivity analysis of input parameters is detailed in the supporting information (Tables S1-S4).

3.1 Bathymetric setting

The model bathymetry was created based on a pockmark field identified in the NW South China Sea, which is observed on multibeam bathymetric data acquired in 2008 by the Guangzhou Marine Geological Survey (Yu et al., 2021). The bathymetric dataset covers an area of ~10,000 km^2 with a water depth range between 300 and 1300 m, a

https://doi.org/10.1002/esp.5610

horizontal resolution of ~100 m (cell size) and a vertical resolution of ~3 m (3‰ of the water depth).

The geometrical parameters, pockmark depth and diameter, of 25 circular pockmarks in the pockmark field were measured using Global Mapper® (Table S5; Fig. 3). The average geometrical parameters were used to create the modelling bathymetries with an isolated pockmark or a pockmark train (in idealized geometries). The maximum erosion depth in Delft3D is 10 meters, while the erosion depth observed at the real-sized pockmarks can be more than 100 meters. In order to simulate the complete erosion process, the diameter and depth of the simulated pockmarks are reduced by ten times compared to the real-sized pockmarks. Therefore, the simulated pockmarks have a diameter of 95 m, a depth of 8 m, and were simulated at a water depth of 85 m, with an initial sediment thickness of 10 m (Table 1). In order to assess the impact of reducing pockmark scale on modeling results, the hydrodynamic simulation (without morphological change) with real-sized and reduced-sized pockmarks was carried out for comparison (Fig. 4). The modelling of two different sized pockmarks was carried out with the same number of layers and input velocity. Therefore, the bottom layer in the modelling of real-sized pockmark is ten times thicker, while the induced horizontal velocity decreases towards to the seabed. Thus, the greater thickness led to a higher horizontal velocity (in average) in the modelling of real-sized pockmark (Fig. 4). More importantly, the modelling results of two different sized pockmarks show a similar hydrodynamic pattern of near-bed currents (i.e. the current in the first layer above the seafloor, in the modeling of this study), both for vertical and horizontal velocities (Fig. 4). Therefore, we assume that the change of pockmark scale does not have a significant impact on the simulation results, and the evolutionary processes dominated by the bottom current erosion on real-sized and reduced-sized pockmarks are comparable.

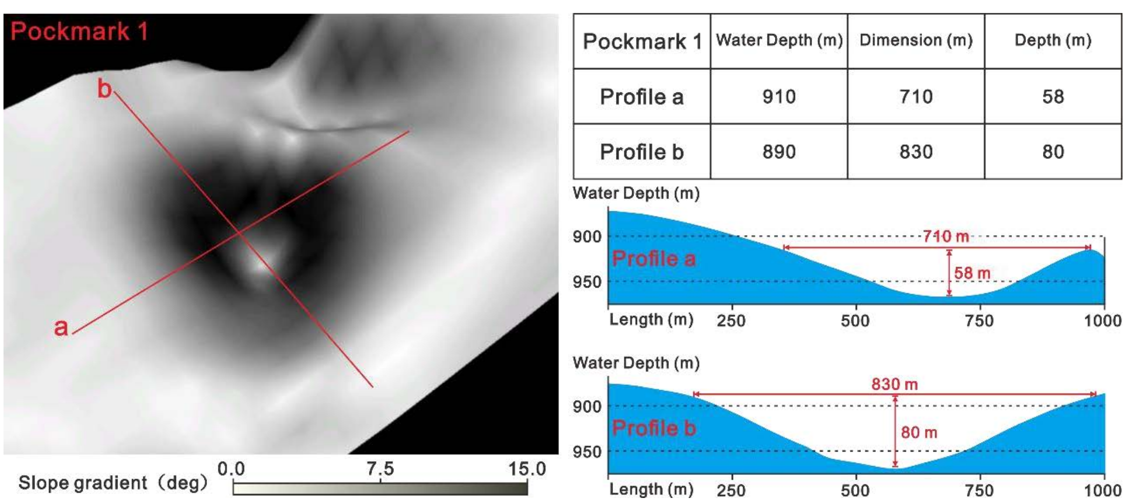

Figure 3. Example showing the geometrical measurement of a single pockmark. 25 pockmarks are measured for the design of the bathymetric setting in this study, and the detail information is shown in Table S5.

Table 1. Initial bathymetric settings of pockmarks used in the numerical simulation.

Scenarios	Real-size pockmark	Single pockmark	Pockmark Train
Grid length	10000 m	1000 m	1200 to 2400 m
Grid width	4000 m	400 m	400 m
Bathymetric resolution	20 m	2 m	2 m
Water depth	850 m	85 m	85 m
Pockmark diameter	950 m	95 m	95 m
Pockmark depth	80 m	8 m	8 m
Angle of the pockmark flanks	~9.5°	~9.5°	~9.5°
Number of pockmarks	1	1	3
Interval distance	-	-	0 to 600 m
Initial sediment thickness	10 m	10 m	10 m
Seafloor slope	0°	0°	0°

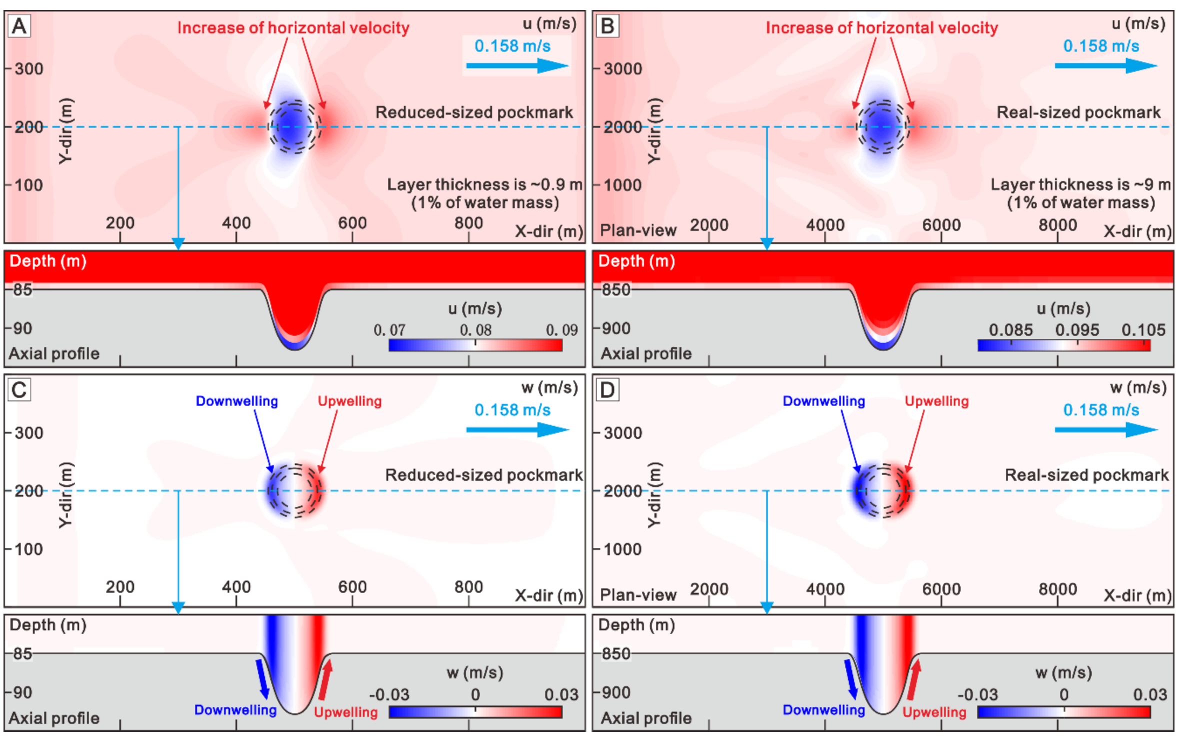

Figure 4. Results of hydrodynamic simulations (without morphological change) of reduced-sized pockmark (A and C) and real-sized pockmark (B and D). The greater thickness of the bottom layer led to a higher horizontal velocity (in average) in the modelling of real-sized pockmark. In general, the real-sized and reduced-sized pockmarks have a similar impact on bottom current actions that: horizontal velocity significantly increases in the upstream and downstream edges of pockmarks, with the upwelling and downwelling formed in the inside slopes of pockmarks. Therefore, the

induced hydrodynamic pattern of near-seafloor currents of the two different scenarios are similar and comparable.

3.2 Numerical model setup

Two sets of simulations were carried out with different purposes in this study (Table 1): the first set of simulations aims to understand the impact of bottom currents above an isolated depression (single pockmark); the second set of simulations looks at pockmark trains with different interval distances to investigate channel inception from discrete depressions (pockmark train). For all of the simulations, the domain was set with two open boundaries, the entrance (left boundary) as a set input velocity with a steady sediment input (0.02 kg/m^3), and the exit (right boundary of the bathymetry) as a constant water level of 0 m. Each simulation lasts 72 hours and contains two phases (Fig. 5). In phase 1, the current velocity increases from 0 to the chosen value (after 6 hours) and then stabilizes (from 6 to 12 hours) (Fig. 5A). Morphological changes only occur during phase 2, when the current velocity is stable (from 12 hours to the end) (Fig. 5B). During the simulation, the initial and final stages indicate the beginning and end of the morphological evolution.

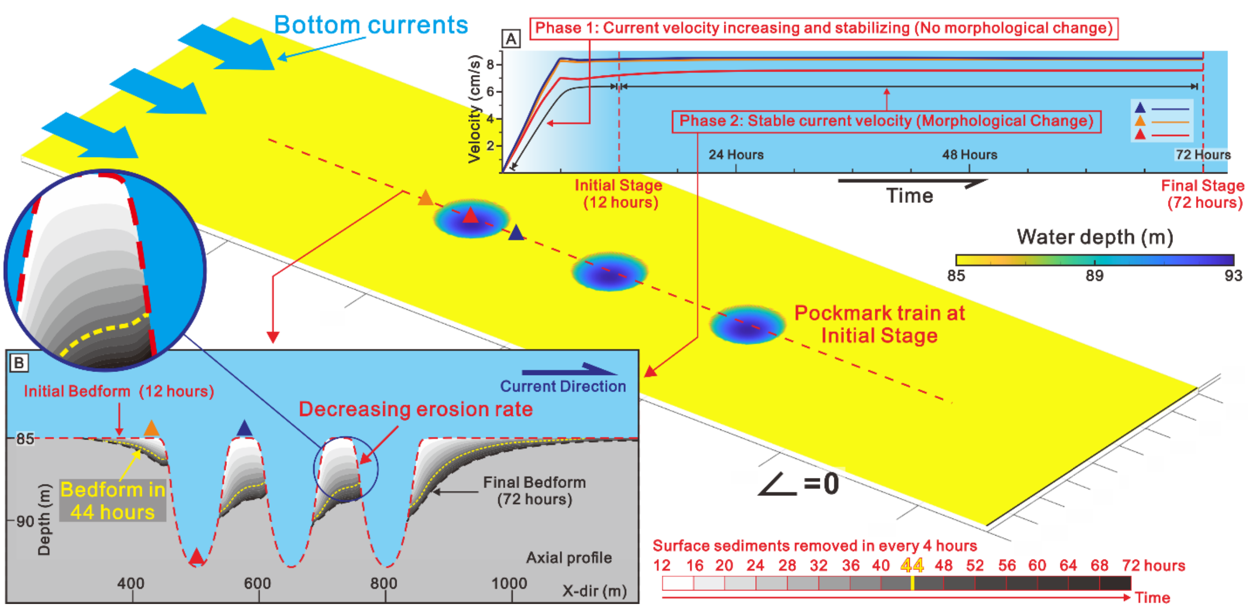

Figure 5. Sketch showing the detailed simulation process composed by two phases. (A) Change of current velocity recorded by three monitoring points (shown as the dark blue, red and orange triangles) at the first layer above seafloor. Current velocity increases to its set value and stabilizes in phase 1 (from 0 to 12 hours), morphological changes only occur in phase 2 which starts at “initial stage” (12 hours) and ends at “final stage” (72 hours). (B) Morphological profile showing the progressive erosion that is characterized by a decreasing trend of erosion rate.

In addition, according to the high-resolution records from drill sites and in-situ observation, bottom-current action and the related morphological evolution is a persistent and long-term process (Bahr et al., 2015; Miramontes et al., 2019b, 2021). In many previous studies, long-term morphological processes have been reconstructed by numerical simulations accelerated by setting a morphological time-scale factor, which amplifies the sediment transport processes based on simulated hydrodynamics (Cayocca, 2001; Dastgheib et al., 2008; Van Der Wegen and Roelvink, 2008; Zhang et al., 2010). In Delft3D, the morphological time-scale factor can also be applied to reduce computational time by applying a scalar multiplier to the sediment continuity equation (Roelvink, 2006; Briere et al., 2011; Morgan et al., 2020). In this study, a sensitivity study of the morphological time-scale factor (MORFAC) has been tested, with MORFAC in the range 1 to 10000 (Table S1). A higher morphological time-scale factor magnifies the feedback of seabed (morphological change), through multiplying the erosion and deposition rate by a constant factor. Importantly, the final results of the tests with different morphological time-scale factors are generally identical, revealing a constant trend for morphological evolution. This is because the imposed hydrodynamics are constant in time during the morphological evolution. In this study, the numerical simulation of bottom current was set with a scaled bathymetry and accelerated by morphological time-scale factor of 3000 (Table S1). This means that the flow velocity and sediment properties have the same scale as in a natural environment, and the morphology and its evolution are scaled in order to accelerate computation time. In this way, the long-term morphological evolution (lasting tens of years) can be effectively reconstructed in the 72 hours simulation time (Fig. 5B).

In this study, we analyze the modelled velocities above pockmarks and the bed shear stress (τ) induced by currents, calculated as (Deltares, 2014):

$$\vec{\tau} = \frac{g\rho_0 \overrightarrow{u_b} |\overrightarrow{u_b}|}{C^2} \quad (1)$$

Where, g (9.81 m/s^2) is the gravity acceleration, ρ_0 (1026 kg/m^3) is the reference density of water, $\overrightarrow{u_b}$ indicates the horizontal velocity of the first layer just above the seabed and C is the Chezy coefficient (set as 34 $m^{1/2}/s$).

4. RESULTS

4.1 Morphological evolution of pockmarks

Following our modelling setup, three representative velocities (0.120, 0.158 and 0.170 m/s) of bottom currents are identified to exemplify three distinctive patterns for the possible evolution of a single pockmark (Fig. 6). From these results, some common patterns can be identified. The highest bed shear stress is located at the streamwise edges of the pockmark, and the lowest at the bottom of the pockmark (Figs. 6E to H).

An input velocity of 0.120 m/s induces a bed shear stress lower than the threshold value for deposition (0.04 N/m^2), resulting in the accumulation of a thin layer of sediment (<0.5 m) on the seafloor and in the formation of small levees at the crosswise banks of the pockmark (Figs. 6B and F). With an input velocity of 0.158 m/s, an erosion is induced at the upstream (to a depth of ca. 1.5 m) and downstream (ca. 5 m) edges of the pockmark. As a consequence, the pockmark elongates 120 m in the upstream direction and 310 m in the downstream direction (Figs. 6C and G). An input velocity of 0.170 m/s induces a bed shear stress higher than the threshold value for erosion in nearly the whole domain, resulting in widespread seafloor erosion and removing most part of the pockmark topography (Figs. 6D and H).

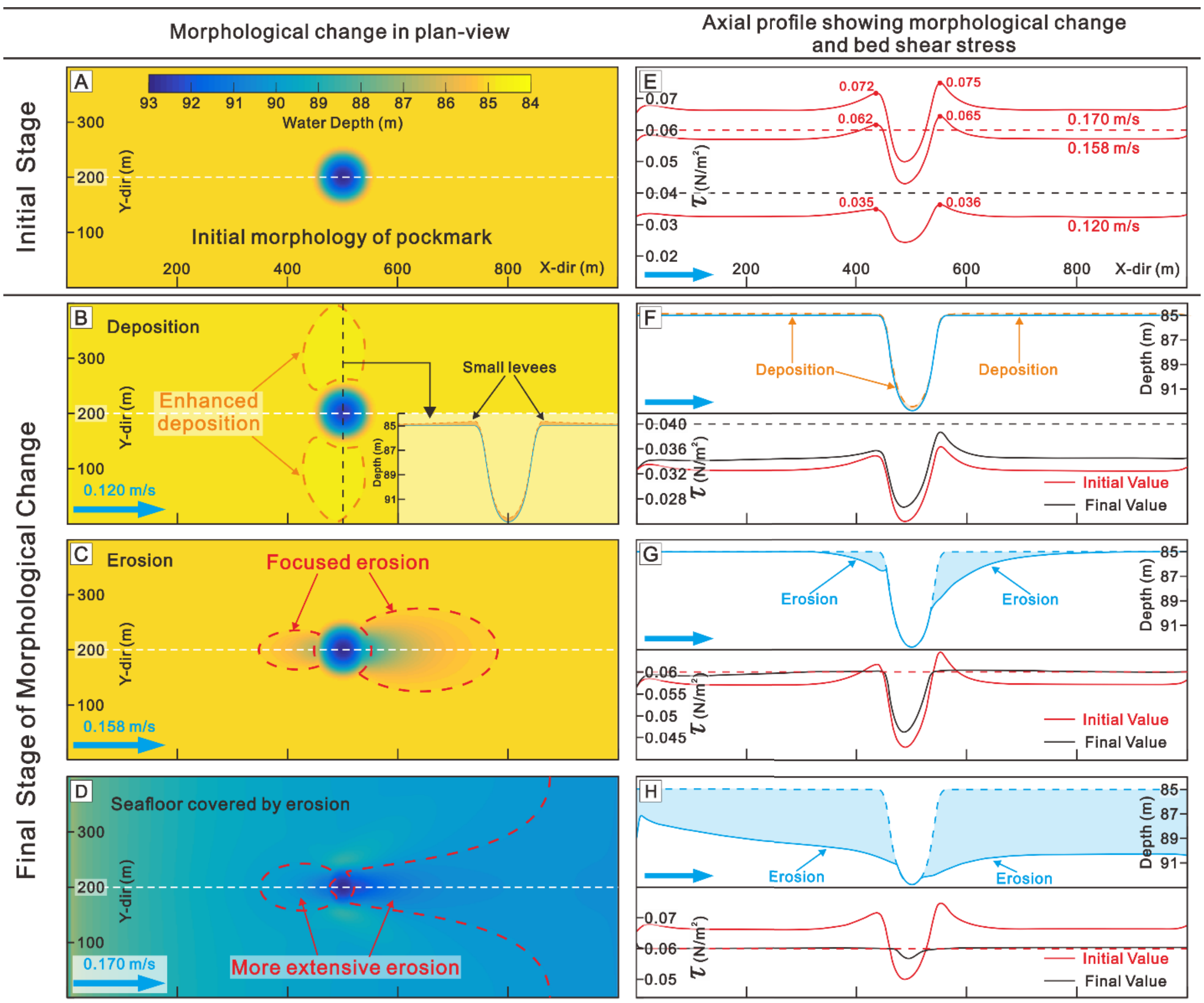

Figure 6. (A, B, C and D) Plan-view pockmark geometries of a single pockmark at the initial (A) and the final stages (B, C and D) of morphological change under different input current velocities. (E) Three different input velocities inducing different bed shear stress (red lines) along the axis of the pockmark at the initial stage of morphological

change. (F, G and H) Axial profiles of the pockmark showing the changes of axial geometries (upper part) and bed shear stresses (lower part) before and after morphological change. In F, G and H, blue and orange dashed lines indicate the erosion and deposition occurred during the morphological change. White dashed lines in plan-view maps indicate the location of profiles. Blue arrows indicate the current direction. In E, F, G and H, red and black dashed lines indicate the threshold values of bed shear stress for erosion and deposition, respectively.

The second set of simulations is carried out with a steady current of 0.158 m/s flowing over a pockmark train composed of three pockmarks with different interval distances (Fig. 7). In all cases, the erosion is focused along the thalweg of the pockmark train, and erodes a wide area of the seafloor on the downstream edge (Figs. 7E to G). During the initial stage, the bed shear stress increases between the pockmarks and reaches a maximum when the pockmarks are directly connected (Fig. 7E). At the final stage, the bed shear stress significantly decreases between the pockmarks and at their streamwise edges, resulting in a decrease of the erosion rate (Figs. 5B and 7E to G). The induced erosion significantly smoothens the seafloor along the pockmark train, reflected by the significant deepening of the seafloor between the pockmarks and by the decrease in gradient of the inside streamwise slopes of pockmarks (Figs. 7E to G), as observed in natural examples (profiles AA' and BB' in Fig. 1). In this simulation, with the input velocity of 0.158 m/s, the maximum distance between pockmarks at which a pockmark train can be coalesced into a channel is ~6 times the diameter of the pockmark (Fig. 7D). In addition, two sets of simulations with pockmarks deviated from the center axis of domain (20 m in total, Fig. S1) showed the influence of pockmarks not directly aligned with the flow. The pockmarks are coalesced along the track of pockmark trains, while the last pockmark (at the end of trails) is still elongated parallel to the current direction (Fig. S1).

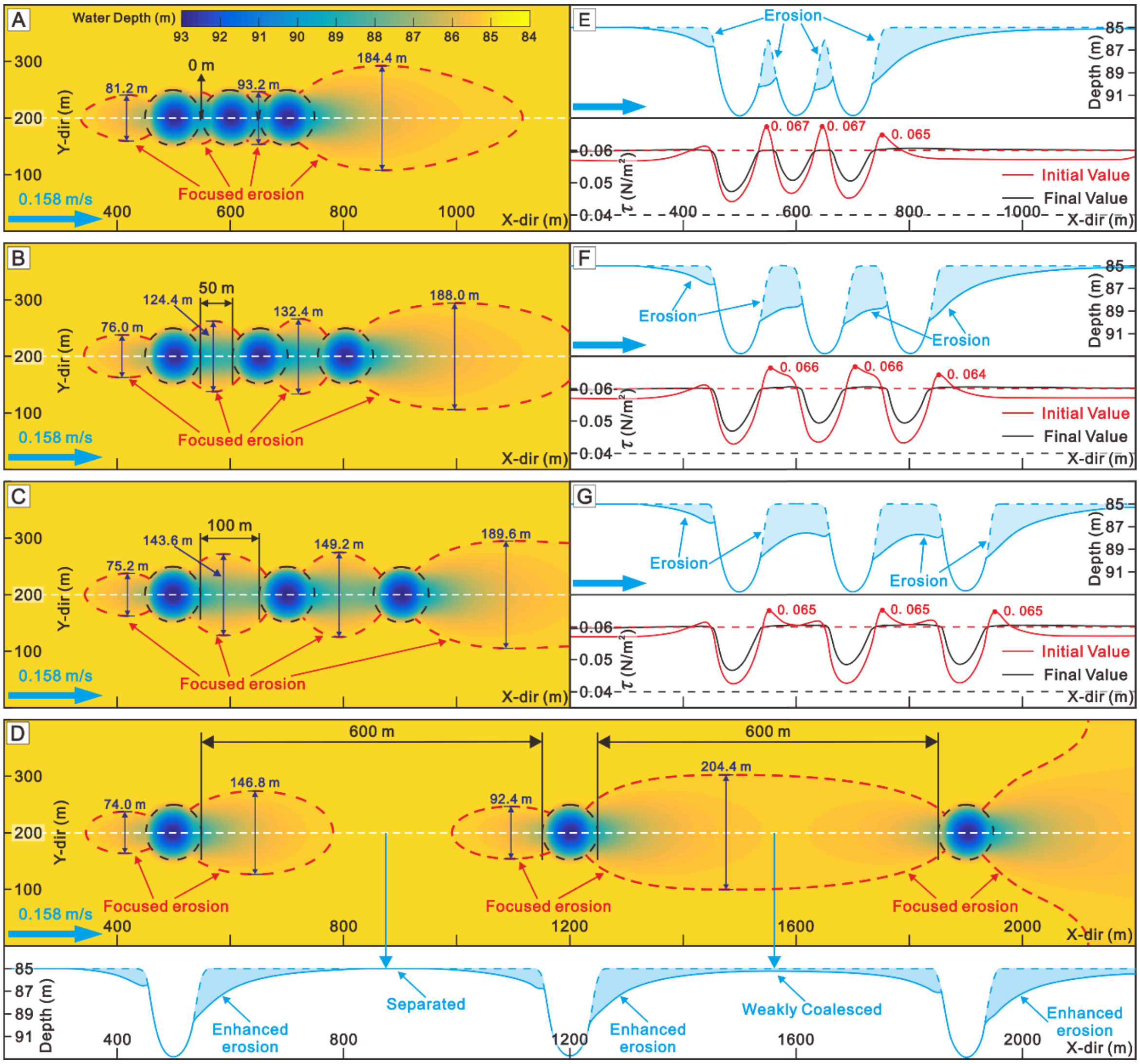

Figure 7. (A, B, C and D) Bathymetric maps showing the plan-view geometry of pockmark trains with different interval distances of 0 m, 50 m, 100 m and 600 m that are eroded by bottom currents (with input current velocity of 0.158 m/s). Black dashed circles indicate the initial edges of pockmarks. (E, F and G) Profiles along the axis of the pockmark train revealing the change of axial morphologies (upper part) and bed shear stresses (lower part) at initial and final stage of morphological change, with the threshold values of bed shear stress for erosion and deposition indicated by red and black dashed lines. The blue dashed lines indicate the eroded seafloor in E, F, G and D. Blue arrows indicate current direction, and the profile location is shown by the white dashed lines in plan-view maps.

4.2 Hydrodynamic change corresponding to morphological evolution

The hydrodynamics of bottom currents not only significantly change upon meeting the depressions of pockmarks, but also keep changing as the pockmarks evolve (Figs. 8 and 9). The horizontal velocity is highest at the streamwise edges of the pockmark, and decrease to lowest at the bottom of the pockmark (Figs. 8A and B). Moreover, the enhancement of horizontal velocity is more remarkable at the downstream edge of the pockmark than at the upstream edge, and the acceleration in horizontal velocity gradually decreases as the pockmark elongates and becomes smooth (Figs. 8A and B). In addition, the upwelling and downwelling of near-bed currents are induced by the inside slopes of the pockmark, and they also diminish with the decline of slope gradient inside the pockmark (Figs. 8C and D). In general, the hydrodynamic change revealed by the velocities is a continuous process, with the general velocity near the seafloor becoming increasingly homogenous as the seafloor morphology changes.

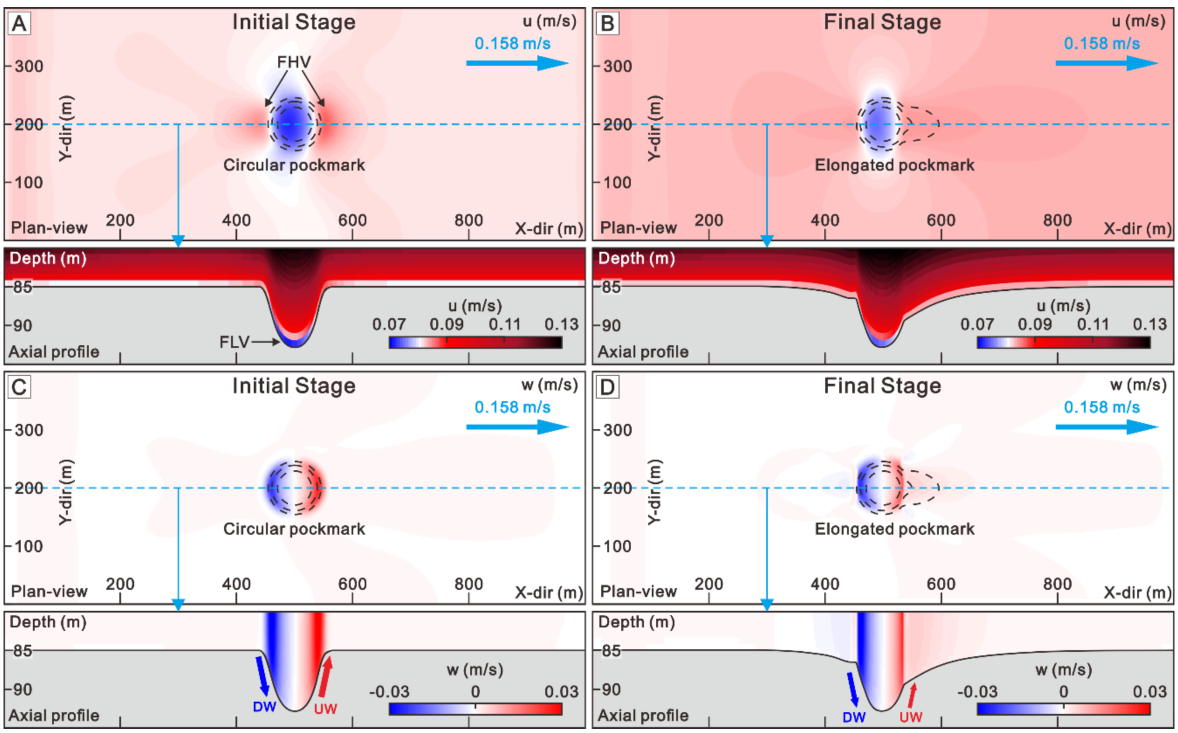

Figure 8. Hydrodynamic change of near-bed currents before (A and C) and after (B and D) morphological change induced by the bottom current (input velocity of 0.158 m/s) over a single pockmark. In A, B, C and D, the circular (at initial stage) and elongated pockmarks (at final stage) are outlined by black dashed contours. The current direction is indicated by the blue arrows, and current velocity is composed by the horizontal (streamwise, A and B, the induced crosswise velocity is less than 0.001 m/s, thus we neglect it) and vertical (C and D) components. The upper parts of A, B, C and D show the velocity of near-bed currents, and the lower parts of each block reveal the velocity profile of near-bed currents (0 to 5 m above the mean seafloor depth, shown as axial profile). u: horizontal streamwise velocity, w: vertical velocity. FHV: focused high velocity, FLV: focused low velocity, DW: downwelling, UW: upwelling.

The hydrodynamics of near-bed currents induced by the pockmark train show significant difference before and after the morphological change (Fig. 9). At the initial stage, the horizontal velocity is significantly higher at the streamwise edges of pockmarks (especially at the interval areas between two neighboring pockmarks), and lower inside the pockmarks and at the crosswise edges (Fig. 9A). At the final stage, as the pockmark train topography smoothens and discrete pockmarks coalesce, the significantly high velocities between the pockmarks decrease and the overall horizontal bottom velocity becomes less variable (Fig. 9B). The flow interacts with the relief of pockmarks, inducing changes in the vertical velocity: downwelling and upwelling form at the upstream and the downstream flanks, respectively (Figs. 9C and D). The distribution of upwelling and downwelling is symmetric at the initial stage (Fig. 9C), but the vertical velocity is significantly reduced at the final stage, especially the upwelling due to the decrease in slope gradient and height of the downstream flanks of the pockmarks (Fig. 9D). Furthermore, the lateral deviation of pockmarks leaded to a skewed distribution of horizontal and vertical velocity, compared with the asymmetrical distribution of velocities induced by the streamwise-aligned pockmarks (Figs. 9 and S1).

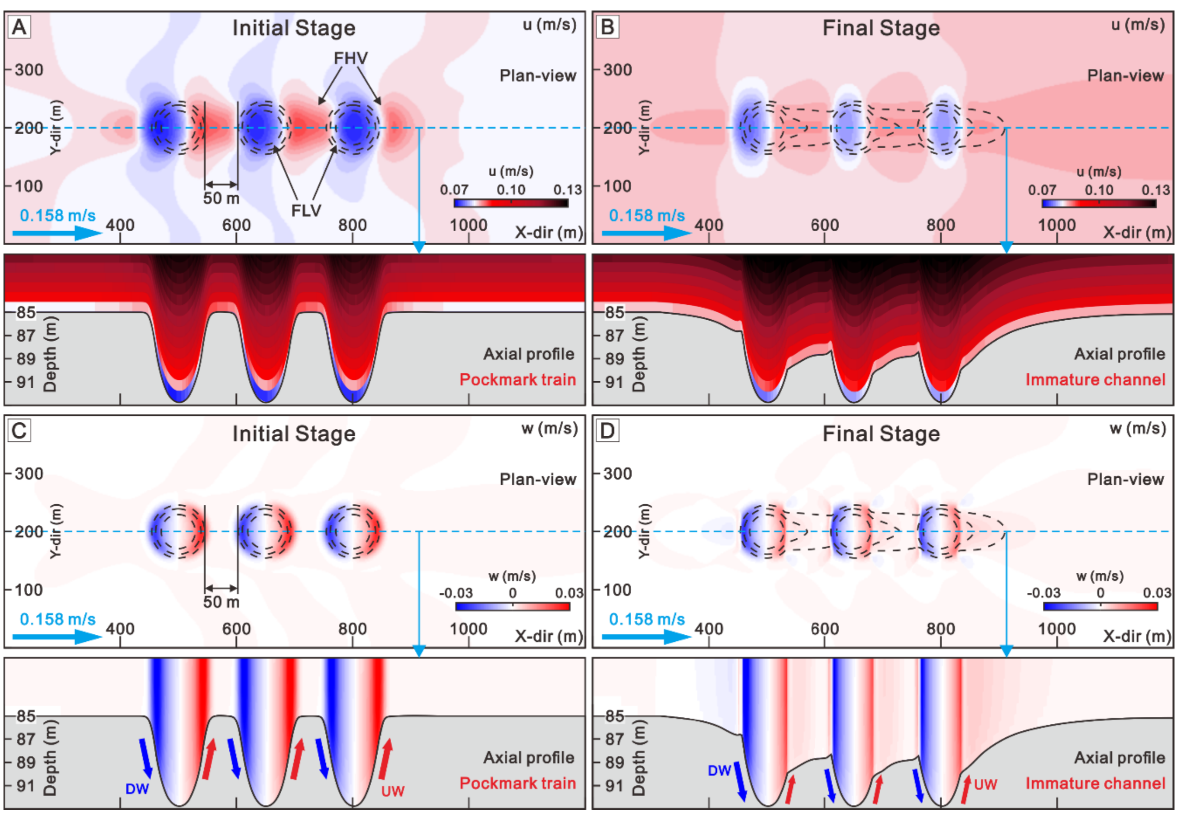

Figure 9. Change of streamwise horizontal velocity (u) and vertical velocity (w) at the initial and final stages of the morphological evolution of a pockmark train. In A, B, C and D, the upper parts show the current velocity in the first layer above the seafloor (~ 0.9

m), and the lower parts reveal the velocity of near-bed currents (0 to 5 m above the mean seafloor elevation). The input current direction is shown as blue arrows. FHV: focused high velocity, FLV: focused low velocity, DW: downwelling, UW: upwelling.

5. DISCUSSION

5.1 Channel inception induced by bottom currents

Turbidite channel inception is formed through the earliest, brief phase of erosion that coalesces depressions related to cyclic steps and produces early negative relief across-slope, allowing the establishment of confined flow and subsequent development of channel-levee systems (Fildani et al., 2013). Channels formed by bottom-current erosion can also originate from discrete depressions (e.g. from pockmarks, Andresen et al., 2008; Kilhams et al., 2011; Yu et al., 2021) (Fig. 1C). However, in contrast to the formation of submarine channels formed by episodic short-lived (hours to days) turbidity currents, bottom currents have to be sustained over a relatively long time (tens or even hundreds of years) in order to generate large-scale current-related erosional and depositional features (Stow et al., 2009; Miramontes et al., 2019b), and thus to coalesce depressions into channels.

The evolution of channel inception induced by bottom-current erosion experiences three stages: pockmark train, immature channel with rough thalweg and mature channel with relatively smooth thalweg (Yu et al., 2021). Based on our results, we can propose a process-based formation of channels by bottoms currents flowing over pockmark trains (Fig. 10). The initial rough topography of the pockmark train will lead to an early erosion phase and channel inception (Figs. 7 and 9). According to the hydrodynamic change of near-bed currents revealed by the simulation results, it is the pre-existence of pockmarks that makes the bottom current velocity significantly increase between the pockmarks or at the streamwise edges of isolated pockmarks (Figs. 8 and 9), resulting in extensive erosion that removes the surface sediment and results in the coalescence of discrete pockmarks or elongation of isolated pockmarks (Figs. 6 and 7). With time, the zones between pockmarks tend to be eroded, smoothening the channel thalweg and, as a result, bed shear stress decreases in these areas, thereby resulting in a slowing or stop of the erosion (Figs. 5B, 6 and 9). Conversely, the bottom current velocity and related bed shear stresses are always the lowest in the center of the depressions (Figs. 6 to 9). This means that under constant currents and sediment supply, the depressions will tend to be infilled, resulting in the reduction of pockmark depth. This has also been observed in natural environments (Yu et al., 2021). Bottom currents in deep-marine environments commonly show strong velocity fluctuations (Miramontes et al., 2019b; Yang et al., 2019; Fuhrmann et al., 2020; Ye et al., 2023), resulting in the alternant occurrence of incision between pockmarks in times of stronger currents and infilling inside the pockmark in times of slower currents (Figs. 6 and 7), jointly contributing to a smoother seabed along the pockmark train.

Active fluid escape may take place in the center of the pockmark (Pilcher and Argent, 2007; Andresen and Huuse, 2011), which can actively inhibit sedimentation and favor channel development. The steep slope gradient and large flank height of pockmarks, maintained by the active fluid escape, contribute to a rugged seabed, which is the key factor inducing channel incision along pockmark trains when current speed accelerates (Figs. 7 and 9). When bottom currents flow through the pockmarks with a low speed and a high sedimentation rate, the pockmarks can be filled up or even buried, as observed in many natural environments (e.g. Dandapath et al., 2010; Betzler et al., 2011). Pockmarks may be distributed randomly or aligned in trains (Fig. 1). Trains of pockmarks usually occur when they are related to faults (Pilcher and Argent, 2007), mass transport deposits (Miramontes et al., 2016) or buried channels (Gay et al., 2003). If pockmarks are not aligned, the disturbances in the bottom current dynamics are isolated in each depression, resulting in isolated elongated pockmarks (Figs. 1B and 6). In contrast, trains of pockmarks that are oriented parallel to the currents affect each other and can coalesce into a channel, especially when the spacing between the depressions is relatively short (Fig. 7). In natural environments, the alignments of pockmark trains are rarely in a completely straight line or fully parallel to the current direction (Fig. 1). Pockmarks distributed with a moderate deviation (or angle) from current direction (e.g. within ~ 20% of pockmark diameter, as the modeling of Fig. S1) can change the velocity distribution of bottom currents, making they follow the 'irregular' pockmark train and finally form a channel (Fig. S1). Therefore, the bottom current erosion, which follows the pockmark alignments, and may alter the main current direction, demonstrates the dominant control of pre-existed bedforms on hydrodynamics of bottom currents.

Both for the single pockmark and pockmark train, the bottom current erosion is stronger on the downstream side than on the upstream pockmark side (Figs. 6 to 9). Therefore, when pockmarks are uniformly-spaced, the pockmarks located at the downstream side will coalesce first, resulting in an upstream development of the channel (Fig. 7D), which has also been observed in the eastern Gulf of Cádiz (León et al., 2014). The number and internal distance between the pockmarks determine the length of the newly formed channel, while the channel width is generally equal to the pockmark diameter perpendicular to the current direction (Figs. 7, 9 and 10). In some of the observed pockmark fields (Fig. 1), the absence of channel inception could be caused by the absence of bottom currents fast enough to enable large erosion (Stow et al., 2009), or by the dispersive distribution of pockmarks.

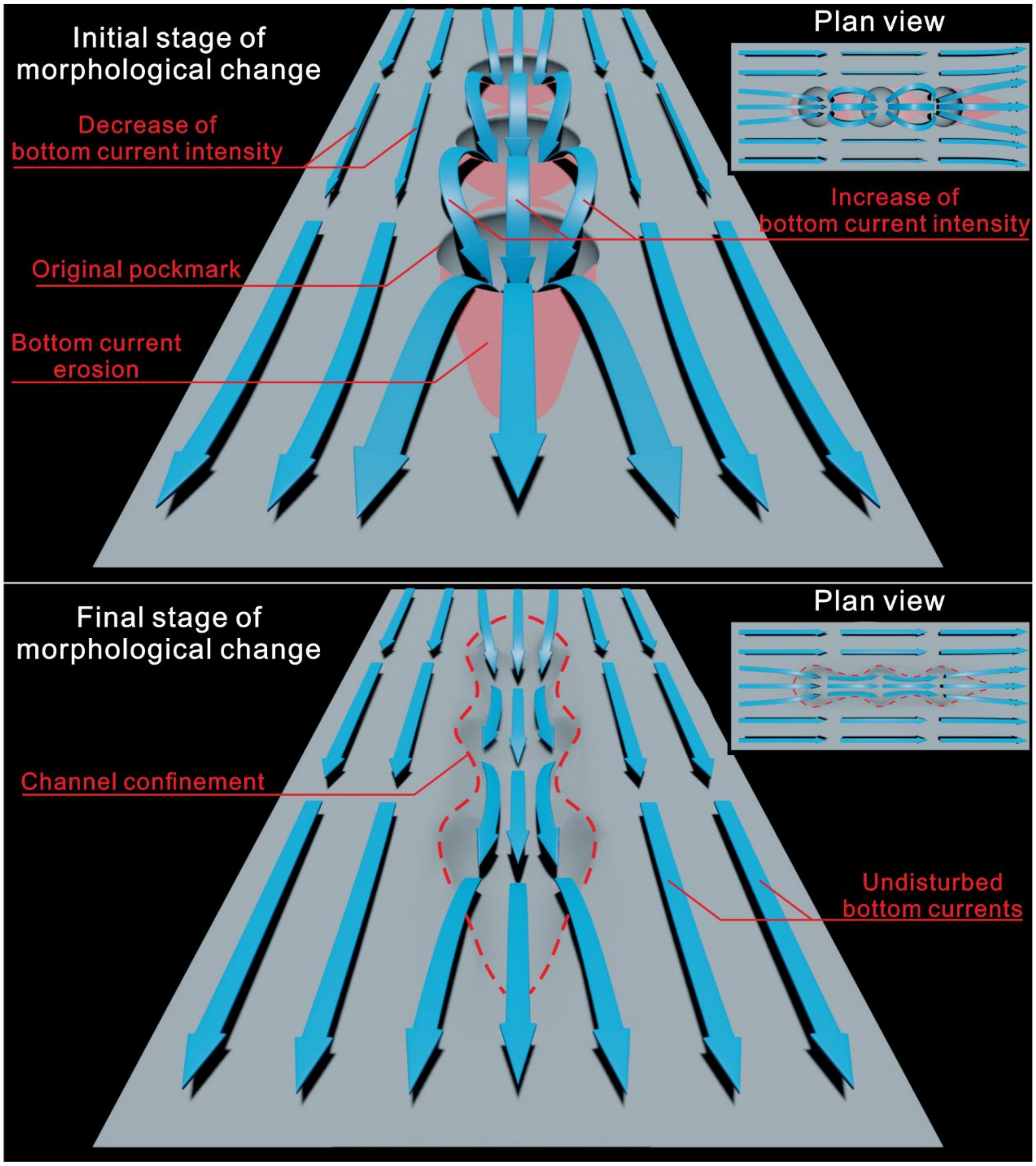

Figure 10. 3D sketch summarizing channel inception induced by bottom currents and revealing the change of bottom current dynamics before and after bottom current erosion, corresponding to the morphological change of the pockmark train.

5.2 Implications of bottom current interaction with a rough seafloor

In deep-water environments, large-scale across-slope depressions, such as submarine canyons, interact with currents flowing alongslope and typically induce local upwellings that pump up nutrients and enhance biological productivity (Fernandez-Arcaya et al., 2017). The interaction of alongslope currents with across-slope canyons and channels can also favor the alongslope redistribution of sediments originally transported by gravity flows and affect the morphology of channels (Miramontes et al., 2020). Furthermore, the influence of bottom currents on the development of many submarine channels (formed by gravity-driven currents) has been widely observed, leading to the formation of mixed (turbidite-contourite) depositional systems around the global continental margins (Rodrigues et al., 2022).

Similar processes of the interaction between pockmarks and bottom currents, as analyzed in our study, can be widely observed on the modern and paleo seafloors. The initial rough topography formed by fluid scape is often modified by bottom currents that enlarge the depressions, form asymmetric sedimentation and crescentic-shaped depressions (Sun et al., 2011; Michaud et al., 2018; Cukur et al., 2019; Wenau et al., 2021). Michaud et al. (2018) and Wenau et al. (2021) observed that sediments were mainly deposited at the upstream flanks and bottom of depressions, which is probably related to the effects of downwelling of bottom currents and low current velocities at the center of the depressions (Figs. 6F, 8 and 9). Under erosive conditions, pockmarks will be elongated along the downstream direction of bottom currents, sometimes inducing channel inception, as observed in the Danish North Sea (Andresen et al., 2008), South China Sea (Yu et al., 2021), NW Mediterranean Sea (Miramontes et al., 2019a), western continental margin of India (Dandapath et al., 2010), Southeastern Brazil (Berton and Vesely, 2018), and Strait of Gibraltar (León et al., 2014) (Fig. 1). The elongated pockmark is initiated from a circular pockmark, while the more intensive erosion at the downstream flank forms the asymmetrical pockmarks thinning in the downstream direction, as initially proposed by Andresen et al. (2008) through the 3D seismic interpretation. This process is fully reconstructed, for the first time, in this study, and we furtherly revealed the enhancement of upwelling at the downstream flank for the downstream elongation of pockmarks (Figs. 8 and 9). With our results, we provide insights for a better interpretation of paleo bottom currents based on the morphology of pockmarks.

In the present study, we focus on the interaction between bottom currents and depressions formed by fluid escape, but similar results could apply to other kind of negative-relief bedforms formed by other factors, such as faulting (Berndt et al., 2012; Gay et al., 2021) and sediment dissolution (Cavailhes et al., 2022; Kluesner et al., 2022). On a nearly aclinal seafloor, the bottom current erosion would be stronger at the downstream flanks (or reaches), shown as the erosion of single pockmark (Fig. 6) or pockmark train (Fig. 7), which is consistent with the current erosion mainly occurred at the downstream of an arc-shaped and elongated depression (with a length of ~ 30 km), at the northern Argentine continental margin (Warnke et al., 2023). In the Grenada Basin (Gay et al., 2021) and the Hatton Basin (Berndt et al., 2012), the wide development of giant polygonal faults on the seabed may induce a stronger bottom current erosion between the neighboring polygons, forming seafloor furrows with a flat bottom. Moreover, large number of mega-depressions (i.e. sinkholes) can be formed by the dissolution of carbonate-rich sediments and surface collapse (Cavailhes et al., 2022; Kluesner et al., 2022), while their interaction between bottom currents is still a poorly known processes, and the difference in the impacts from sinkholes and pockmarks on bottom current actions are also worthy of thorough investigation. In addition, the development of subsurface structures, i.e. faults, diapir, gas chimney and buried channels, determines the distribution of pockmarks and other heterogeneities on the seafloor, subsequently controlling the inception and development of pockmark-related channels (Pilcher and Argent, 2007; Sun et al., 2011; Cartwright and Santanmarina, 2015; Chen et al., 2018).

The complex hydrodynamics at depressions does not only affect sediment transport and the depression morphological evolution, it can also play an important role in the structure of benthic communities. Webb et al. (2009) observed higher abundance of suspension feeders on the slope of pockmarks, suggesting the presence of relatively strong currents and high particle resuspension, in agreement with our model results (Figs. 9 and 10). The interplay between seabed morphology, local hydrodynamics and habitat distribution is observed over bedforms such as marine dunes (Damveld et al., 2018), but it is poorly understood in depressions in deep-sea environments. Our modelling results show the potential implications of the interaction of bottom currents with depressions, and we hope they will motivate future studies that can measure these processes in natural environments.

6. CONCLUSION

The evolutionary process of bottom-current-related channel inception from pockmarks are reconstructed herein from numerical simulations based on observed morphological data, sediment cores and current measurements. The simulation results effectively reveal the possible morphological evolution of pockmarks and hydrodynamic change of bottom currents during the processes of channel inception. The pre-existence of pockmarks alters the hydrodynamics of bottom currents, leading to seafloor erosion focused along the thalweg of pockmark trains, especially at the streamwise edges of pockmarks. The induced upwelling of bottom current generates a stronger erosion, resulting in a greater elongation, at the downstream edge of the pockmark than on its upstream side. When the current velocity is constant and stable, the bottom current erosion is strongest at the initial stage of morphological change, and it will gradually decrease as the seafloor gets smoother along the pockmark train. Furthermore, the bottom-current erosion can be enhanced if the interval distance between pockmarks is reduced, and the coalescence of pockmarks may not happen if the distance between pockmarks is too wide (i.e. >6 times the diameter of the pockmark in this study). This study illustrates the reshaping processes of pockmarks by bottom currents and reveals the detailed processes of channel inception dominated by the influence of bottom currents.

Acknowledgments

This work is financially supported by Guangdong Basic and Applied Basic Research Foundation (2020B1515020016) and National Natural Science Foundation of China (41876054). Dr. Wei Li is funded by CAS Pioneer Hundred Talents Program

(Y8SL011001). We thank University of Chinese Academy of Sciences for providing the scholarship to support the research stay of Dr. Kaiqi Yu at the University of Bremen. Dr. Alice Lefebvre is funded through the Cluster of Excellence ›The Ocean Floor – Earth's Uncharted Interface‹. We thank the Editor Stuart Lane, the associate editor and two anonymous reviewers for their constructive comments that helped us improve our manuscript.

REFERENCES

Andresen, K.J. & Huuse, M. (2011) 'Bulls-eye' pockmarks and polygonal faulting in the Lower Congo Basin: Relative timing and implications for fluid expulsion during shallow burial. *Marine Geology*, 279(1-4): 111-127. Avaliable from: https://doi.org/10.1016/j.margeo.2010.10.016.

Andresen, K.J., Huuse, M. & Clausen, O.R. (2008) Morphology and distribution of Oligocene and Miocene pockmarks in the Danish North Sea–implications for bottom current activity and fluid migration. *Basin Research*, 20(3), 445-466. Avaliable from: https://doi.org/10.1111/j.1365-2117.2008.00362.x.

Astakhov, A.S. (2004) Grain size composition of bottom sediments from East Asian marginal seas, core Ast-87063, *PANGAEA*. Avaliable from: https://doi.org/10.1594/PANGAEA.137251.

Audsley, A., Bradwell, T., Howe, J.A. & Baxter, J.M. (2019) Distribution and classification of pockmarks on the seabed around western Scotland. *Journal of Maps*, 15(2), 807-817. Avaliable from: https://doi.org/10.1080/17445647.2019.1676320.

Bahr, A., Kaboth, S., Jiménez-Espejo, F.J., Sierro, F.J., Voelker, A.H.L., Lourens, L., Röhl, U., Reichart, G.J., Escutia, C., Hernández-Molina, F.J., Pross, J. & Friedrich, O. (2015) Persistent monsoonal forcing of Mediterranean Outflow Water dynamics during the late Pleistocene. *Geology*, 43(11), 951-954. Avaliable from: https://doi.org/10.1130/G37013.1.

Berndt, C., Jacobs, C., Evans, A., Gay, A., Elliott, G., Long, D. & Hitchen, K. (2012) Kilometre-scale polygonal seabed depressions in the Hatton Basin, NE Atlantic Ocean: Constraints on the origin of polygonal faulting. *Marine Geology*, 332-334: 126-133. Avaliable from: http://dx.doi.org/10.1016/j.margeo.2012.09.013.

Berton, F. & Vesely, F.F. (2018) Origin of buried, bottom current-related comet marks and associated submarine bedforms from a Paleogene continental margin, southeastern Brazil. *Marine Geology*, 395, 347-362. Avaliable from: https://doi.org/10.1016/j.margeo.2017.11.015.

Betzler, C., Lindhorst, S., Hübscher, C., Lüdmann, T., Fürstenau, J. & Reijmer, J. (2011) Giant pockmarks in a carbonate platform (Maldives, Indian Ocean). *Marine Geology*, 289(1-4), 1-16. Avaliable from: https://doi.org/10.1016/j.margeo.2011.09.004

Briere, C., Giardino, A., & van der Werf, J. (2011) Morphological modeling of bar dynamics with DELFT3d: the quest for optimal free parameter settings using an automatic calibration technique. *Coastal Engineering Proceedings: sediment*, 1(32), 1-12. Avaliable from: https://doi.org/10.9753/icce.v32.sediment.60.

Cartwright, J. & Santamarina, C. (2015) Seismic characteristics of fluid escape pipes in sedimentary basins: implications for pipe genesis. *Marine and Petroleum Geology*, 65, 126-140. Avaliable from: https://doi.org/10.1016/j.marpetgeo.2015.03.023.

Cavailhes, T., Gillet, H., Guiastrennec-Faugas, L., Mulder, T. & Hanquiez, V. (2022) The abyssal giant sinkholes of the Blake Bahama Escarpment: evidence of focused deep-ocean carbonate dissolution. *Geomorphology*, 398. Avaliable from: https://doi.org/10.1016/j.geomorph.2021.108058.

Cayocca, F. (2001) Long-term morphological modeling of a tidal inlet: the Arcachon Basin, France. *Coastal engineering*, 42(2), 115-142. Avaliable from: https://doi.org/10.1016/S0378-3839(00)00053-3.

Chen, J., Song, H., Guan, Y., Pinheiro, L.M. & Geng, M. (2018) Geological and oceanographic controls on seabed fluid escape structures in the northern Zhongjiannan Basin, South China Sea. *Journal of Asian Earth Sciences*, 168: 38-47. Avaliable from: http://dx.doi.org/10.1016/j.dsr2.2015.11.007.

Covault, J.A., Kostic, S., Paull, C.K., Ryan, H.F. & Fildani, A. (2014) Submarine channel initiation, filling and maintenance from sea ‐ floor geomorphology and morphodynamic modelling of cyclic steps. *Sedimentology*, 61(4), 1031-1054. Avaliable from: https://doi.org/10.1111/sed.12084.

Cukur, D., Kong, G.-S., Chun, J.-H., Kang, M.-H., Um, I.-K., Kwon, T., Johnson, S.Y. & Kim, K.-O. (2019) Morphology and genesis of giant seafloor depressions on the southeastern continental shelf of the Korean Peninsula. *Marine Geology*, 415, 105966. Avaliable from: https://doi.org/10.1016/j.margeo.2019.105966.

Damveld, J.H., van der Reijden, K.J., Cheng, C., Koop, L., Haaksma, L.R., Walsh, C.A., Soetaert, K., Borsje, B.W., Govers, L.L. & Roos, P.C. (2018) Video transects reveal that tidal sand waves affect the spatial distribution of benthic organisms and sand ripples. *Geophysical research letters*, 45, 11,837-11,846. Avaliable from: https://doi.org/10.1029/2018GL079858.

Dandapath, S., Chakraborty, B., Karisiddaiah, S.M., Menezes, A., Ranade, G., Fernandes, W., Naik, D.K. & Raju, K.P. (2010) Morphology of pockmarks along the western continental margin of India: employing multibeam bathymetry and backscatter data. *Marine and Petroleum Geology*, 27, 2107-2117. Avaliable from: https://doi.org/10.1016/j.marpetgeo.2010.09.005.

Dastgheib, A., Roelvink, J.A. & Wang, Z.B. (2008) Long-term process-based morphological modeling of the Marsdiep Tidal Basin. *Marine Geology*, 256(1-4), 90-100. Avaliable from: https://doi.org/10.1016/j.margeo.2008.10.003.

Davies, A.J., Duineveld, G.C., van Weering, T.C., Mienis, F., Quattrini, A.M., Seim, H.E., Bane, J.M. & Ross, S.W. (2010) Short-term environmental variability in cold-water coral habitat at Viosca Knoll, Gulf of Mexico. *Deep Sea Research Part I: Oceanographic Research Papers*, 57, 199-212. Avaliable from: https://doi.org/10.1016/j.dsr.2009.10.012.

de Leeuw, J., Eggenhuisen, J.T. & Cartigny, M.J. (2016) Morphodynamics of submarine channel inception revealed by new experimental approach. *Nature communications*, 7, 1-7. Avaliable from: https://doi.org/10.1038/ncomms10886.

Deltares. (2014) User manual Delft3D ‐ FLOW. Delft, *The Netherlands: Deltares*, p. 329-331.

Fernandez-Arcaya, U., Ramirez-Llodra, E., Aguzzi, J., Allcock, A.L., Davies, J.S., Dissanayake, A., Harris, P., Howell, K., Huvenne, V.A. & Macmillan-Lawler, M. (2017) Ecological role of submarine canyons and need for canyon conservation: a review. *Frontiers in Marine Science*, 4, 5. Avaliable from: https://doi.org/10.3389/fmars.2017.00005.

Fildani, A., Hubbard, S. M., Covault, J. A., Maier, K. L., Romans, B. W., Traer, M., & Rowland, J. C. (2013) Erosion at inception of deep-sea channels. *Marine and Petroleum Geology,* 41, 48-61. Avaliable from: https://doi.org/10.1016/j.marpetgeo.2012.03.006.

Fuhrmann, A., Kane, I. A., Clare, M. A., Ferguson, R. A., Schomacker, E., Bonamini, E. & Contreras, F. A. (2020) Hybrid turbidite-drift channel complexes: An integrated multiscale model. *Geology*, 48(6), 562-568. Avaliable from: https://doi.org/10.1130/G47179.1.

Gay, A., Lopez, M., Cochonat, P., Sultan, N., Cauquil, E. & Brigaud, F. (2003) Sinuous pockmark belt as indicator of a shallow buried turbiditic channel on the lower slope of the Congo Basin, West African Margin. *Geological Society, London, Special Publications*, 216, 173-189. Avaliable from: https://doi.org/10.1144/GSL.SP.2003.216.01.12.

Gay, A., Padron, C., Meyer, S., Beaufort, D., Oliot, E., Lallemand, S., Marcaillou, B., Philippon, M., Cornée, J.J., Audemard, F., Lebrun, J.F., Klingelhoefer, F., Mercier de Lepinay, B., Münch, P., Garrocq, C., Boucard, M. & Schenini, L. (2021) Elongated Giant Seabed Polygons and Underlying Polygonal Faults as Indicators of the Creep Deformation of Pliocene to Recent Sediments in the Grenada Basin, Caribbean Sea. *Geochemistry, Geophysics, Geosystems*, 22(12). Avaliable from: https://doi. org/10.1029/2021GC009809.

Habgood, E.L., Kenyon, N.H., Masson, D.G., Akhmetzhanov, A., Weaver, P.P., Gardner, J. & Mulder, T. (2003) Deep‐water sediment wave fields, bottom current sand channels and gravity flow channel‐lobe systems: Gulf of Cadiz, NE Atlantic. *Sedimentology*, 50, 483-510. Avaliable from: https://doi.org/10.1046/j.1365-3091.2003.00561.x.

Kilhams, B., McArthur, A., Huuse, M., Ita, E. & Hartley, A. (2011) Enigmatic large-scale furrows of Miocene to Pliocene age from the central North Sea: current-scoured pockmarks?. *Geo-Marine Letter*s, 31(5), 437-449. Avaliable from: https://doi.org/10.1007/s00367-011-0235-1.

Kluesner, J.W., Silver, E.A., Bangs, N.L., Ranero, C.R., Nale, S., Gibson, J. & McIntosh, K.D. (2022) Mega-Depressions on the Cocos Ridge: Links Between Volcanism, Faults, Hydrothermal Circulation, and Dissolution. *Geochemistry, Geophysics, Geosystems*, 23(8). Avaliable from: https://doi. org/10.1029/2022GC010370.

León, R., Somoza, L., Medialdea, T., González, F.J., Gimenez-Moreno, C.J. & Pérez-López, R. (2014) Pockmarks on either side of the Strait of Gibraltar: formation from overpressured shallow contourite gas reservoirs and internal wave action during the last glacial sea-level lowstand? *Geo-Marine Letters*, 34(2-3): 131-151. Avaliable from: https://doi.org/10.1007/s00367-014-0358-2.

Lesser, G.R., Roelvink, J.v., van Kester, J.T.M. & Stelling, G. (2004) Development and validation of a three-dimensional morphological model. *Coastal engineering*, 51, 883-915. Avaliable from: https://doi.org/10.1016/j.coastaleng.2004.07.014.

Liu, J., Clift, P.D., Yan, W., Chen, Z., Chen, H., Xiang, R. & Wang, D. (2014) Modern transport and deposition of settling particles in the northern South China Sea: Sediment trap evidence adjacent to

Xisha Trough. *Deep Sea Research Part I: Oceanographic Research Papers*, 93: 145-155. Avaliable from: http://dx.doi.org/10.1016/j.dsr.2014.08.005.

Liu, J., Xiang, R., Chen, Z., Chen, M., Yan, W., Zhang, L. & Chen, H. (2013) Sources, transport and deposition of surface sediments from the South China Sea. *Deep Sea Research Part I: Oceanographic Research Papers*, 71: 92-102. Avaliable from: https://doi.org/10.1016/j.dsr.2012.09.006.

Liu, Q., Kaneko, A. & Jilan, S. (2008) Recent progress in studies of the South China Sea circulation. *Journal of Oceanography*, 64, 753-762. Avaliable from: https://doi.org/10.1007/s10872-008-0063-8.

Michaud, F., Collot, J.-Y., Ratzov, G., Proust, J.-N., Dano, A., Lebrun, J., Hernández, M., Loayza, G., Khaoulani, A. & Stoll, Y. (2018) A honeycomb seafloor morphology in carbonate sediment of the Carnegie Ridge (offshore Ecuador): Formation and potential geodynamic significance. *Geology*, 46, 979-982. Avaliable from: https://doi.org/10.1130/G45285.1.

Miramontes, E., Cattaneo, A., Jouet, G., Thereau, E., Thomas, Y., Rovere, M., Cauquil, E. & Trincardi, F. (2016) The Pianosa contourite depositional system (northern Tyrrhenian Sea): Drift morphology and Plio-Quaternary stratigraphic evolution. *Marine Geology*, 378, 20-42. Avaliable from: https://doi.org/10.1016/j.margeo.2015.11.004.

Miramontes, E., Eggenhuisen, J.T., Jacinto, R.S., Poneti, G., Pohl, F., Normandeau, A., Campbell, D.C. & Hernández-Molina, F.J. (2020) Channel-levee evolution in combined contour current–turbidity current flows from flume-tank experiments. *Geology*, 48, 353-357. Avaliable from: https://doi.org/10.1130/G47111.1.

Miramontes, E., Garreau, P., Caillaud, M., Jouet, G., Pellen, R., Hernández-Molina, F.J., Clare, M.A. & Cattaneo, A. (2019a) Contourite distribution and bottom currents in the NW Mediterranean Sea: Coupling seafloor geomorphology and hydrodynamic modelling. *Geomorphology*, 333, 43-60. Avaliable from: https://doi.org/10.1016/j.geomorph.2019.02.030.

Miramontes, E., Penven, P., Fierens, R., Droz, L., Toucanne, S., Jorry, S.J., Jouet, G., Pastor, L., Jacinto, R.S. & Gaillot, A. (2019b) The influence of bottom currents on the Zambezi Valley morphology (Mozambique Channel, SW Indian Ocean): In situ current observations and hydrodynamic modelling. *Marine Geology*, 410, 42-55. Avaliable from: https://doi.org/10.1016/j.margeo.2019.01.002.

Miramontes, E., Thiéblemont, A., Babonneau, N., Penven, P., Raisson, F., Droz, L., Jorry, S.J., Fierens, R., Counts, J.W., Wilckens, H., Cattaneo, A. & Jouet, G. (2021) Contourite and mixed turbidite-contourite systems in the Mozambique Channel (SW Indian Ocean): Link between geometry, sediment characteristics and modelled bottom currents. *Marine Geology*, 437. Avaliable from: https://doi.org/10.1016/j.margeo.2021.106502.

Morgan, J. A., Kumar, N., Horner-Devine, A. R., Ahrendt, S., Istanbullouglu, E. & Bandaragoda, C. (2020) The use of a morphological acceleration factor in the simulation of large-scale fluvial morphodynamics. *Geomorphology*, 356, 107088. Avaliable from: https://doi.org/10.1016/j.geomorph.2020.107088.

Peakall, J. & Sumner, E.J. (2015) Submarine channel flow processes and deposits: A process-product perspective. *Geomorphology*, 244, 95-120. Avaliable from: https://doi.org/10.1016/j.geomorph.2015.03.005.

Peakall, J., Amos, K.J., Keevil, G.M., Bradbury, P.W. & Gupta, S. (2007) Flow processes and sedimentation in submarine channel bends. *Marine and Petroleum Geology*, 24, 470-486. Avaliable from: https://doi.org/10.1016/j.marpetgeo.2007.01.008.

Picard, K., Radke, L.C., Williams, D.K., Nicholas, W.A., Siwabessy, P.J., Howard, F.J., Gafeira, J., Przeslawski, R., Huang, Z. & Nichol, S. (2018) Origin of high density seabed pockmark fields and their use in inferring bottom currents. *Geosciences*, 8, 195. Avaliable from: https://doi.org/10.3390/geosciences8060195.

Pilcher, R., & Argent, J. (2007) Mega-pockmarks and linear pockmark trains on the West African continental margin. *Marine Geology*, 244(1-4), 15-32. Avaliable from: https://doi.org/10.1016/j.margeo.2007.05.002.

Posamentier, H.W. & Kolla, V. (2003) Seismic geomorphology and stratigraphy of depositional elements in deep-water settings. *Journal of sedimentary research*, 73, 367-388. Avaliable from: https://doi.org/10.1306/111302730367.

Quan, Q. & Xue, H. (2018) Layered model and insights into the vertical coupling of the South China Sea circulation in the upper and middle layers. *Ocean Modelling*, 129, 75-92. Avaliable from: https://doi.org/10.1016/j.ocemod.2018.06.006.

Rebesco, M., Hernández-Molina, F.J., Van Rooij, D. & Wåhlin, A. (2014) Contourites and associated sediments controlled by deep-water circulation processes: State-of-the-art and future considerations. *Marine Geology*, 352, 111-154. Avaliable from: https://doi.org/10.1016/j.margeo.2014.03.011.

Rodrigues, S., Hernández-Molina, F.J., Fonnesu, M., Miramontes, E., Rebesco, M. & Campbell, D.C. (2022) A new classification system for mixed (turbidite-contourite) depositional systems: Examples, conceptual models and diagnostic criteria for modern and ancient records. *Earth-Science Reviews*, 230. Avaliable from: https://doi.org/10.1016/j.earscirev.2022.104030.

Roelvink, J. A. (2006) Coastal morphodynamic evolution techniques. *Coastal engineering*, 53(2-3), 277-287. Avaliable from: https://doi.org/10.1016/j.coastaleng.2005.10.015.

Stow, D.A. & Mayall, M. (2000) Deep-water sedimentary systems: New models for the 21st century. *Marine and Petroleum Geology*, 17, 125-135. Avaliable from: https://doi.org/10.1016/S0264-8172(99)00064-1.

Stow, D.A.V., Hernández-Molina, F.J., Llave, E., Sayago-Gil, M., Díaz del Río, V. & Branson, A. (2009) Bedform-velocity matrix: The estimation of bottom current velocity from bedform observations. *Geology*, 37(4), 327-330. Avaliable from: https://doi.org/10.1130/G25259A.1.

Sun, Q., Wu, S., Hovland, M., Luo, P., Lu, Y. & Qu, T. (2011) The morphologies and genesis of mega-pockmarks near the Xisha Uplift, South China Sea. *Marine and Petroleum Geology*, 28(6): 1146-1156. Avaliable from: https://doi.org/10.1016/j.marpetgeo.2011.03.003.

Van Der Wegen, M. & Roelvink, J.A. (2008) Long-term morphodynamic evolution of a tidal embayment using a two-dimensional, process-based model. *Journal of Geophysical Research*, 113(C3). Avaliable from: https://doi.org/10.1029/2006JC003983.

Warnke, F., Schwenk, T., Miramontes, E., Spiess, V., Wenau, S., Bozzano, G., Baqués, M. & Kasten, S. (2023) Evolution of complex giant seafloor depressions at the northern Argentine continental margin

(SW Atlantic Ocean) under the influence of a dynamic bottom current regime. *Frontiers in Earth Science*, 11. Avaliable from: https://doi.org/10.3389/feart.2023.1117013.

Webb, K.E., Barnes, D.K. & Plankea, S. (2009) Pockmarks: Refuges for marine benthic biodiversity. *Limnology and Oceanography*, 54, 1776-1788. Avaliable from: https://doi.org/10.4319/lo.2009.54.5.1776.

Wenau, S., Spiess, V. & Zabel, M. (2021) Giant seafloor depressions caused by slope failures and bottom currents on the Namibia continental margin. *Geochemistry, Geophysics, Geosystems*, 22, e2020GC009548. Avaliable from: https://doi.org/10.1029/2020GC009548.

Wilckens, H., Miramontes, E., Schwenk, T., Artana, C., Zhang, W., Piola, A.R., Baques, M., Provost, C., Hernández-Molina, F.J. & Felgendreher, M. (2021) The erosive power of the Malvinas Current: Influence of bottom currents on morpho-sedimentary features along the northern Argentine margin (SW Atlantic Ocean). *Marine Geology*, 439, 106539. Avaliable from: https://doi.org/10.1016/j.margeo.2021.106539.

Wilckens, H., Schwenk, T., Lüdmann, T., Betzler, C., Zhang, W., Chen, J., Hernández-Molina, F.J., Lefebvre, A., Cattaneo, A., Spieß, V. & Miramontes, E. (2023) Factors controlling the morphology and internal sediment architecture of moats and their associated contourite drifts. *Sedimentology*. Avaliable from: https://doi.org/10.1111/sed.13093.

Yang, Y., Xu, C., Li, S. & He, Y. (2019) Ship-mounted ADCP data for ocean currents in the South China Sea (2009 – 2012): *Science Data Bank*, (March 8, 2019). Avaliable from: http://www.doi.org/10.11922/sciencedb.740.

Ye, R., Zhou, F., Ma, X., Zhou, B., Zeng, D., Liu, C., Meng, Q., Lin, F., Xu, M., Li, H. & Shou, L. (2023) Energetic Bottom Current at the Equatorial Gap of the Ninety East Ridge in the Indian Ocean Based on Mooring Data. *Journal of Geophysical Research: Oceans*, 128, e2022JC018974. Avaliable from: https://doi. org/10.1029/2022JC018974.

Yi, L., Jian, Z., Liu, X., Zhu, Y., Zhang, D., Wang, Z. & Deng, C. (2018) Astronomical tuning and magnetostratigraphy of Neogene biogenic reefs in Xisha Islands, South China Sea. *Sci Bull (Beijing)*, 63(9): 564-573. Avaliable from: https://doi.org/10.1016/j.scib.2018.04.001.

Yin, S., Hernández-Molina, F.J., Lin, L., Chen, J., Ding, W. & Li, J. (2021) Isolation of the South China Sea from the North Pacific Subtropical Gyre since the latest Miocene due to formation of the Luzon Strait. *Scientific reports*, 11, 1-9. Avaliable from: https://doi.org/10.1038/s41598-020-79941-4.

Yu, K., Miramontes, E., Alves, T.M., Li, W., Liang, L., Li, S., Zhan, W. & Wu, S. (2021) Incision of submarine channels over pockmark trains in the South China Sea. *Geophysical Research Letters*, 48, e2021GL092861. Avaliable from: https://doi.org/10.1029/2021GL092861.

Zhang, L., Wang, R., Chen, M., Liu, J., Zeng, L., Xiang, R. & Zhang, Q. (2015) Biogenic silica in surface sediments of the South China Sea: Controlling factors and paleoenvironmental implications. *Deep Sea Research Part II: Topical Studies in Oceanography*, 122: 142-152. Avaliable from: http://dx.doi.org/10.1016/j.dsr2.2015.11.008.

Zhang, W., Harff, J., Schneider, R. & Wu, C. (2010) Development of a modelling methodology for simulation of long-term morphological evolution of the southern Baltic coast. *Ocean Dynamics*, 60(5), 1085-1114. Avaliable from: https://doi.org/10.1007/s10236-010-0311-5.

Zhong, Y., Chen, Z., Li, L., Liu, J., Li, G., Zheng, X., Wang, S. & Mo, A. (2017) Bottom water hydrodynamic provinces and transport patterns of the northern South China Sea: Evidence from grain size of the terrigenous sediments. *Continental Shelf Research*, 140, 11-26. Avaliable from: https://doi.org/10.1016/j.csr.2017.01.023.